ISSN 1029-9599, Physical Mesomechanics, 2014, Vol. 17, No. 4, pp. 304–310. © Pleiades Publishing, Ltd., 2014.
Original Text © H.X. Nguyen, E. Teidelt, V.L. Popov, S. Fatikow, 2014, published in Fizicheskaya Mezomekhanika, 2014, Vol. 17, No. 3, pp. 77–83.

# Dynamic Tangential Contact of Rough Surfaces in Stick-Slip Microdrives: Modeling and Validation Using the Method of Dimensionality Reduction

**H. X. Nguyen[1]*, E. Teidelt[2], V. L. Popov[2, 3, 4], and S. Fatikow[1]**

[1] *University of Oldenburg, Oldenburg, 26121 Germany*
[2] *Technische Universität Berlin, Berlin, D-10623 Germany*
[3] *National Research Tomsk State University, Tomsk, 634050 Russia*
[4] *National Research Tomsk Polytechnic University, Tomsk, 634050 Russia*
* *e-mail: xuan.ha.nguyen@uni-oldenburg.de*

Received February 17, 2014

**Abstract**—The dynamic tangential contact of rough surfaces of frictional elements of a stick-slip microdrive is theoretically investigated. By applying the method of dimensionality reduction, the contact areas of the frictional partners are modeled such that the physical properties of the contact can be fully considered and the influence of the roughness is taken into account. The dynamics of the microscopic rough contact is combined with a macroscopic movement of the drive runner in a hybrid dynamic simulation. The numerical results show a good agreement with experimental data. Furthermore, an analytical relation between maximal tangential contact displacement and normal force applied on the contact is analyzed, allowing the contact behavior to be theoretically predicted.

**DOI:** 10.1134/S1029959914040079

*Keywords*: stick-slip microdrive, piezoelectric actuator, tangential contact, roughness, method of dimensionality reduction

## 1. INTRODUCTION

Piezo-actuated stick-slip microdrives have been applied widely and effectively in miniaturized micro- and nanoposition and manipulation systems. The two main advantages of such drives are the simplification in design consisting of a few parts and the very good working characteristics. The drives exhibit motions of theoretical unlimited traveling range accompanied by a very high resolution of several nanometers. The motion principle of stick-slip drives was firstly introduced by Pohl [1]. The motion consists of sequences of a stick phase and a slip phase. During the stick phase, the mobile part, called the runner, moves slowly along with the actuators due to the static friction force between the runner and the actuators. This phase is followed by the slip phase with a rapid movement of the actuators in the opposite direction, such that the runner cannot fully follow this movement and slides with respect to the actuators. Thus, a step-wise motion of the runner is obtained.

For the last three decades there have been many prototypes and systems based on the stick-slip principle. A review of such devices is given in [2] and an analysis of the state-of-the-art attempts to model the friction in the contacts of the drives can be found in [3]. It is known that the friction model for the microcontacts of the drives is important and has been the focus of recent investigations. With stick-slip microdrives, the simple Coulomb's friction law alone cannot cover important behavior of friction in microcontacts such as presliding, maximum relative tangential deformation of the contact before full slip occurs. Consequently, more sophisticated friction models, which are based on the extension of Dahl's single state friction law [4], have been developed and applied for the stick-slip microdrives. These include the LuGre model [5, 6], the EPM model [7, 8] and the CEIM model [9]. The application of these models is simple as most of the input parameters are empirically chosen and the models can be directly used in a dynamic simulation of the stick-slip drives.

However, the frictional behavior of the microcontacts are not determined by the empirical parameters, but by the contact area and its dynamics. Recently in [10] a

new approach for modeling dynamically changing contact areas has been introduced. This approach can consequently compute the friction force in the contact areas. By applying the method of dimensionality reduction [11–16], the dynamic tangential contacts of a stick-slip microdrive working as a force generating device were investigated. Simulations of the new model show that there is a good agreement between numerical findings and experimental data without using any empirical parameters. For further details of the method and results, the readers are encouraged to refer to this earlier publication [10]. The subject of this paper is the optimization of the model in order to reduce the remaining deviations in the simulation results. We extend the presented model such that the contact area is modeled as a contact of self-affine fractal rough surfaces by again applying the method of dimensionality reduction. The microscopic model of the contacts is combined with the macroscopic movement of the drive runner in a dynamic simulation. It will be shown that the numerical results match very well with the experimental data if typical parameters for roughness are taken into account.

## 2. EXPERIMENTAL INVESTIGATIONS

The method of force generation using stick-slip drives was first presented by Edeler [9]. In [10], for the validation of our new friction model, we extended the device created by Edeler such that important influencing parameters (e.g. radius of frictional contacts, preloads, and control amplitude of the driving signal) can be independently controlled and investigated. In this section, the experimental implementation is shortly described.

Figure 1 shows a schematic view of the experimental test stand, with which the runner of a linear stick-slip drive is held in position and actuated by six piezoelectric actuators. The piezoelectric actuators are driven by a saw-tooth signal with a maximal driving amplitude of $300\,V_{pp}$ and a slew-rate of 150 V/μs. A discontinuous change of voltage in shape of a saw-tooth driving signal rotates ruby hemispheres of radius $R = 0.5$ mm. The moving displacement of the center of contact of each ruby hemisphere, further denoted as actuation amplitude, is measured by the changing voltages applied and results in possible amplitudes from 0 to 160 nm. The preload, which determines the normal force on the contacts and therefore also influences the contact behavior, is applied to the drive by using an external spring. The level of the applied preload is varied from 0.1 to 1 N. The generated force is measured by the load cell (Honeywell Model 31) and the position of the runner is tracked by the laser interferometer (SIOS SP-S120). All the material and geometrical data used for the experiments as well as further simulations are listed in Table 1.

**Table 1.** Material and geometrical data used for experiments and numerical simulations

| | |
|---|---|
| Young's modulus $E_1$ (runner, steel X90CrMoV18) | 210 GPa |
| Young's modulus $E_2$ (hemisphere, ruby) | 370 GPa |
| Poisson's ratio $\nu_1$, $\nu_2$ | 0.3 |
| Friction coefficient $\mu$ | 0.3 |
| Ruby sphere radius | 0.5 mm |
| Runner mass $m$ | 3 g |

Figure 2 shows the results of generated force with four selected levels of preload ranging from 0.1 to 1.0 N. For each preload, the generated force depends on the actuation amplitude. The graphs show two characteristics. Firstly, the force is only generated if the actuation amplitude is large enough. The amplitude, below which no

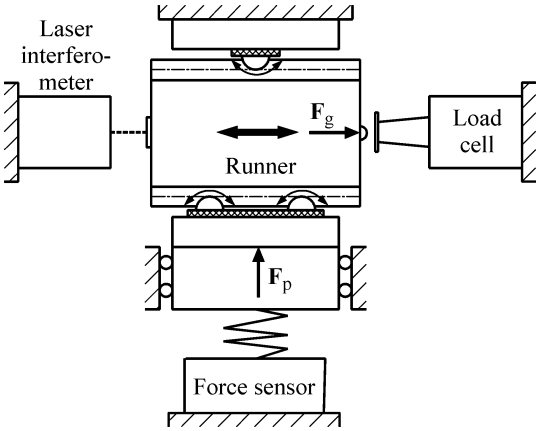


**Fig. 1.** Schematic of the test stand.

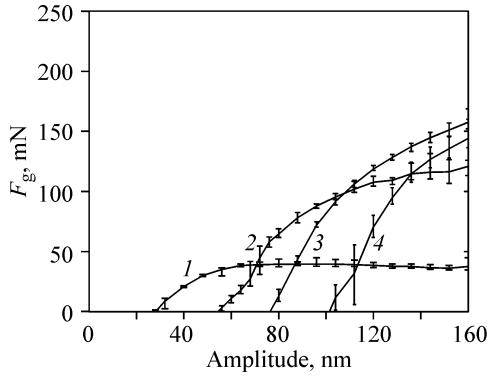


**Fig. 2.** Dependence of the generated forces on preload and actuation amplitude. Preload 0.1 (*1*), 0.4 (*2*), 0.7 (*3*), 1.0 N (*4*).

force is generated, is defined as 0-amplitude [9]. This phenomenon is explained by the limit of elastic contact deformation (pre-sliding) and determined by the preload and contact configuration. If the actuation amplitude is below the 0-amplitude, the runner cannot overcome the tangential contact deformation. Thus, it just vibrates around the equilibrium position and cannot perform stick-slip motion. As a result, no net displacement of the runner is obtained and therefore no force is generated. Since the elastic deformation of the contact is proportional with the preload, the 0-amplide increases with the rising preload. Secondly, for the small preload (e.g. $F_p$ = 0.1 N), after reaching the 0-amplitude, the generated force increases with rising actuation amplitude until a saturation status is reached. With higher preload, no saturation status is obtained and the generated force increases with the rising actuation amplitude.

It can be concluded that with different preload levels different levels of the generated force are obtained. The generated forces depend on preload and actuation amplitude, and therefore on the contact mechanics of the frictional partners. The 0-amplitude is of importance. In the following sections the modeling of friction of rough contacts will be considered to numerically describe the dependence between the generated force, actuation amplitude and preload.

## 3. MODELING AND SIMULATION

The microscopic model presented in [10], was extended such that the roughness is taken into account and applied to all contact areas between the runner and ruby hemisphere surfaces. In fact, roughness in these contacts is mostly contributed by the runner surfaces, since the runner is fabricated through the wire electrical discharge machining method without surface polishing. In contrast, the ruby hemisphere surface is well polished. However, for the convenience of theoretical derivation, these rough contacts are equivalently modeled as contacts between a rigid rough hemisphere, superposing a hemisphere and a flat rough surface, and a smooth elastic half-space.

It has been shown that the method of dimensionality reduction can exactly model normal contacts with randomly self-affine fractal roughness [17–19]. In this paper, this theory is applied and extended to dynamically describe tangential rough contacts between the ruby hemispheres and the runner surfaces by the microscopic model. This microscopic model will be then coupled with the macroscopic one which describes the overall runner movement in a dynamic simulation.

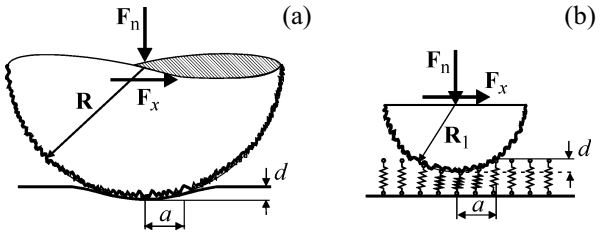


**Fig. 3.** Three-dimensional contact between a rigid sphere with superposed self-affine fractal surface and an elastic half-space (a); a one-dimensional contact between equivalent "rough parabola" and an elastic foundation (b).

### *3.1. The Tangential Contact of Rough Surfaces in the Method of Dimensionality Reduction*

The tangential contact between a rigid sphere and an elastic half-space with a randomly self-affine fractal roughness is considered. To model this configuration a sphere with superposed random self-affine fractal surface as shown in Fig. 3a can be used.

The surface topography of the sphere is characterized by the power spectrum $C_{2D}(\mathbf{q})$. For the self-affine fractal surfaces, the spectral density depends on the magnitude $q$ of the wave vector $\mathbf{q}$ according to the power law:

$$C_{2D}(q) = \text{const} \times \left( \frac{q}{q_0} \right)^{-2H-2}, \qquad (1)$$

where $H$ is the Hurst exponent ranging from 0 to 1. This constant is directly related to the fractal dimension of an original two-dimensional surface $D_f = 3 - H$. The surface topography is then calculated through the power spectrum:

$$h(\mathbf{x}) = \sum_q B_{2D}(\mathbf{q}) \exp(i(\mathbf{q} \cdot \mathbf{x} + \phi(\mathbf{q}))) \qquad (2)$$

with

$$B_{2D}(\mathbf{q}) = \frac{2\pi}{L} \sqrt{C_{2D}(\mathbf{q})} = \bar{B}_{2D}(-\mathbf{q}), \qquad (3)$$

and random phase $\phi(\mathbf{q}) = -\phi(\mathbf{q})$ in the interval $[0, 2\pi)$.

By applying the method of dimensionality reduction, the above-described rough contact can be equivalently modeled by a one-dimensional one, where a "rough parabola" is in contact with an elastic foundation (see Fig. 3b). The elastic foundation has a set of springs with distance $\Delta x$. It is noticeable that these springs have a normal and a tangential stiffness in order to map the properties of a normal and a tangential contact. To be equivalent to the initial three-dimensional contact, the following four conditions must be satisfied.

Firstly, the normal stiffness $\Delta k_z$ and the tangential stiffness $\Delta k_x$ of each spring must be chosen according to

$$\Delta k_z = E^* \Delta x \text{ and } \Delta k_x = G^* \Delta x, \quad (4)$$

where $E^*$ denotes the effective elastic modulus which depends on the Young's moduli $E_1$, $E_2$, and Poisson's ratios $\nu_1$, $\nu_2$ of the contacting bodies, respectively, and it is

$$\frac{1}{E^*} = \frac{1-\nu_1^2}{E_1} + \frac{1-\nu_2^2}{E_2}, \quad (5)$$

and $G^*$ is the effective shear modulus, defined as

$$\frac{1}{G^*} = \frac{2-\nu_1}{4G_1} + \frac{2-\nu_2}{4G_2}. \quad (6)$$

Secondly, the radius of the one-dimensional "rough parabola" $R_1$ must be [12]

$$R_1 = \frac{R}{2}. \quad (7)$$

Thirdly, to receive the similar roughness properties as the three-dimensional one, the rule for generating one-dimensional power spectrum must be created. As proposed in [13, 16], the qualitative arguments for the choice of proper one-dimensional system are that the mean square values of height for a two-dimensional $\langle h^2 \rangle_{2D}$ and one-dimensional system $\langle h^2 \rangle_{1D}$ must be the same. We have

$$\langle h^2 \rangle_{2D} = 2\pi \int_0^\infty q C_{2D}(q) \mathrm{d}q, \quad (8)$$

$$\langle h^2 \rangle_{1D} = 2 \int_0^\infty q C_{1D}(q) \mathrm{d}q. \quad (9)$$

Therefore, the one-dimensional power spectrum is chosen to

$$C_{1D}(q) = \pi q C_{2D}(q). \quad (10)$$

In the case of self-affine fractal rough surface from Eqs. (1) and (10), we have

$$C_{1D}(q) = \text{const} \times \left( \frac{q}{q_0} \right)^{-2H-1}. \quad (11)$$

The surface topography of the equivalent one-dimensional system in the form of a "rough line" is then calculated through the power spectrum

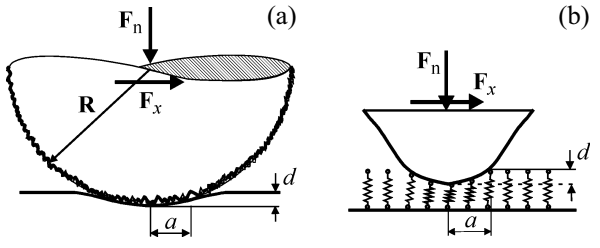


**Fig. 4.** Three-dimensional contact between a rigid sphere with superposed self-affine fractal surface and an elastic half-space (a); a one-dimensional contact between equivalent profile and an elastic foundation (b).

$$h(x) = \sum_q B_{1D}(q) \exp(i(qx + \phi(q))) \quad (12)$$

with

$$B_{1D}(q) = \sqrt{\frac{2\pi}{L} C_{1D}(q)} = \bar{B}_{1D}(-q). \quad (13)$$

Finally, the rough parabola is a superposition of a parabola and a rough line:

$$u_z(x) = \frac{x^2}{2R_1} + h(x). \quad (14)$$

### *3.2. Equivalence between Rough Self-affine Surfaces and Symmetrically Rotational Surfaces*

The numerical calculation for the reduced contact described in Fig. 3b still costs much simulation time, especially when it is combined with the dynamic simulation of the macro-system, since a larger number of rough surfaces must be averaged for representative results. In [14], it is shown that the three-dimensional contact having symmetrically rotational bodies can be exactly mapped to equivalent one-dimensional contact by applying the method of dimensionality reduction to a normal contact. The equivalent mapping for tangential contacts is shown in [20]. In this section, we will show that the numerical simulations of rough contact can be simpler and how the contact of rough surface is replaced by an equivalent symmetrically rotational contact.

The roughness of the self-affine fractal surface can be equivalently replaced by a symmetrically rotational indenter having the form:

$$f(r) = Q_{3D} r^n \text{ with } n = H \in (0, 1]. \quad (15)$$

In Eq. (15) $Q_{3D}$ is the prefactor relating to the roughness parameters and determined from the Pohrt–Popov rule [20]:

$$Q_{3D} = \left( \frac{2(H+1)}{1.9412L} \right)^{H+1} \frac{(H+1)L}{2H\kappa(H)} h, \quad (16)$$

where $L$ is the system length and in the case of a sphere $L = 2R$, $h$ is the root mean square of the roughness; $\kappa(H)$ is the prefactor depending on the Hurst exponent.

Furthermore, by applying the Hess rule [14], the three-dimensional symmetrically rotational contact in form (15) can be mapped to one-dimensional one, in which the equivalent profile is defined by:

$$g(x) = Q_{1D} |x|^H \text{ with } Q_{1D} = Q_{3D} \kappa(H). \quad (17)$$

Now, one can equivalently model the contact of a rough sphere by the superposition of the contact of a smooth sphere and a symmetrically rotational shape and map it to one-dimensional system as shown in Eq. (18) and exemplarily depicted in Fig. 4b:

$$u_z(x) = x^2 / (2R_1) + Q_{1D} |x|^H. \quad (18)$$

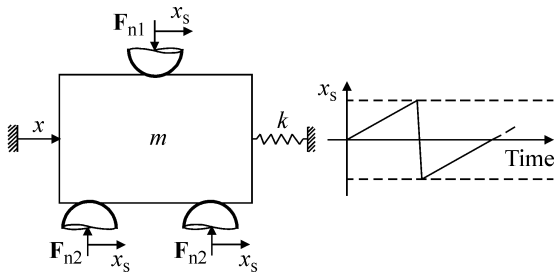


**Fig. 5.** Model for the stick-slip drive with six contact points, only three of six contacts are depicted.

### *3.3. Macroscopic Model*

The physical model of the force generating drive described in Sect. 2 is shown in Fig. 5. The drive is modeled as a mass–spring system, in which the runner with a mass *m* is in contact with six ruby hemispheres (two above and four below). Only three of six contacts are represented. The normal forces applied on the contacts are calculated from the preload through the geometrical factor:

$$F_{n1} = \frac{\sqrt{2}}{2} F_p \text{ and } F_{n2} = \frac{\sqrt{2}}{4} F_p. \quad (19)$$

The translational saw-tooth displacement of the ruby hemispheres and the stick-slip motion of the runner are described by $x_s$ and $x$, respectively. The contact between the runner and the load cell is modeled by a spring with stiffness $k$. The generated force $F_g$ applied to the load cell is calculated by multiplying the stiffness $k$ and the runner displacement $x$. The second Newton law then yields

$$m\ddot{x} = -kx + F_r, \quad (20)$$

where $F_r$ is the sum of friction force between the hemispheres and the runner computed by the microscopic model.

### *3.4. Microscopic Model and Dynamic Simulation*

The friction force is now computable, if the contact is modeled as an equivalent contact via the method of dimensionality reduction as in Fig. 4b. Solving the differential equation (20) in each time step, one has to compute the overall friction force

$$F_r = \sum_i f_{x,i}, \quad (21)$$

where the summation includes all tangential spring forces of all six contacts. To compute this force, due to the runner and hemisphere motion, all springs undergo a horizontal relative displacement $u_x = x - x_s$. Each spring is then either in the stick or the slip state. Say $u_z$ is the displacement of each spring in the vertical direction, then the spring forces in the tangential and vertical direction are $f_x = \Delta k_x u_x$ and $f_z = \Delta k_z u_z$. A spring slips if the stick condition no longer holds: $f_x = \Delta k_x u_x > \mu f_z$. Then the spring force becomes $f_x = \mu f_z$ and the tangential displacement changes accordingly. This implies that for each time step, the condition of each spring must be checked and changed if necessary.

The dynamic movement of the drive was simulated in MATLAB® by a hybrid model combining the macroscopic and microscopic models. In the simulations, for each time step of the dynamic simulation of the macroscopic movement of the runner, the friction forces of the microscopic tangential contacts between the rough ruby hemispheres and the runner are numerically computed via the method of dimensionality reduction.

## 4. VALIDATION

The quality of the introduced friction model is validated by comparing the numerical and experimental results. The simulations with preloads in the range from 0.1 to 1 N were implemented, with the geometrical and material data of Table 1. Furthermore, as a first approximation, the Hurst exponent for the roughness of technical surface was set to value $H = 0.7$ and the prefactor in Eq. (18) was empirically determined to $Q_{1D} = 4.4478 \times 10^{-4}$. These chosen parameters are based on the root mean square of the roughness with selected value $h = 1.1221$ μm (see Eqs. (16) and (17)). This selection logically relates to the fact that the root-mean-square roughness of the runner surfaces fabricated by wire electrical discharge machining has a scale around 1 μm. For the sake of clarity, only results for three selected preloads are illustrated in Fig. 6a. Other experimental data do not indicate different results in comparing the experimental and numerical findings. Additionally, it is important to see how the extended friction model is improved in comparison with the model presented in [10]. Therefore, the results obtained in [10] without the effect of surface roughness are also presented in Fig. 6b.

It is clearly visible that the simulations with the rough contact model in Fig. 6a can predict the overall tendencies of the generated force regarding the 0-amplitude and the saturation of the force. The 0-amplitude is excellently matched and the level of generated force is qualitatively agreed with experimental data. Whereas the simulations with smooth contact model in Fig. 6b show a qualitative agreement with the experiment in which the much larger discrepancies both in 0-amplitude and the generated force are detected.

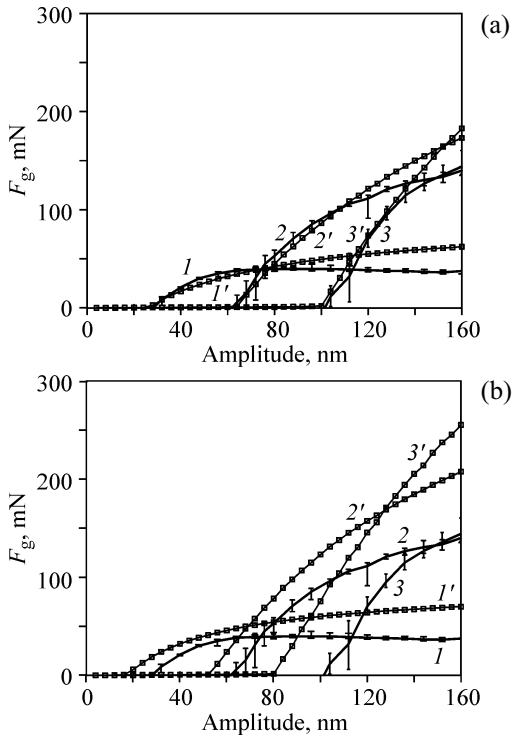


**Fig. 6.** Comparison of numerical simulations (0.1 (*1′*), 0.5 (*2′*), 1.0 N (*3′*)) and experiments (0.1 (*1*), 0.5 (*2*), 1.0 N (*3*)), the generated force is presented as the function of actuation amplitude and preload: results of the model extended in this paper (rough contact) (a); results of the model presented in [10] (smooth contact) (b).

The graphs in Fig. 6b show that the 0-amplitudes in simulation are always smaller than those in experiment, whereas in Fig. 6a the simulated 0-amplitudes fit well with the experimental one. This illustrates well that the contacts in reality can be much better represented by a rough surface interaction.

The simulations of both models still show a discrepancy in level of generated force, when the actuation amplitude becomes larger. This can be explained by the use of the ideal saw-tooth signal in the simulations. In fact, the rapid change from slow to fast status of the saw-tooth-like movement of the actuator (contact point) is not as sharp as it is assumed in the simulations.

Furthermore, the 0-amplitude has been explained to relate to the tangential elastic contact deformation. It is therefore interesting to analyze the relation between maximum tangential displacement $u_{x,\max}$ and normal force $F_n$ applied on the rough contact analytically.

The interrelation of the normal and tangential contact problems has been presented in [21], in which the maximum tangential displacement $u_{x,\max}$ is depended on the maximum normal displacement $u_{z,\max}$ by the rule

$$u_{x,\max} = \mu C_M u_{z,\max}, \tag{22}$$

where $C_M$ is the Cattaneo–Mindlin factor depending on the ratio of the normal contact stiffness $k_z$ to the tangential contact stiffness $k_x$

$$C_M = \frac{k_z}{k_x} = \frac{E^*}{G^*}. \tag{23}$$

The relation in Eq. (22) permits explicitly to determine $u_{x,\max}$ by the solution of the normal contact problem in which $u_{z,\max}$ is the indentation depth *d*. Furthermore, the relation between normal force $F_n$ and indentation depth *d* for the contact described in Fig. 4b is defined according to Eq. (10.58) of [20]

$$F_n = 2E^* \int_0^a [d - u_z(x)]\mathrm{d}x$$
$$= 2E^* \left[ da - \frac{a^3}{3R} - Q_{1D} \frac{a^{H+1}}{H+1} \right], \tag{24}$$

where *a* is contact radius determined from Eq. (18) with the condition $u_z(a) = d$:

$$d = \frac{a^2}{R} + Q_{1D} a^H. \tag{25}$$

From Eqs. (22), (24), and (25) the analytical relation of $u_{x,\max}$ and $F_n$ is obtained.

For the convenience of comparison with experimental data, the analytical dependency of $u_{x,\max}$ on preload $F_p$ is presented in Fig. 7. For this instance, the normal force in Eq. (24) is $F_{n2}$ from Eq. (19). Here, it is assumed that the maximum tangential displacement of the drive contacts before complete sliding is determined by the contact with the lower normal force (the contact at the runner bottom). Also, the results of the dynamic simulation in Sect. 3 and the experiment for the dependency of the 0-amplitude on preload are plotted.

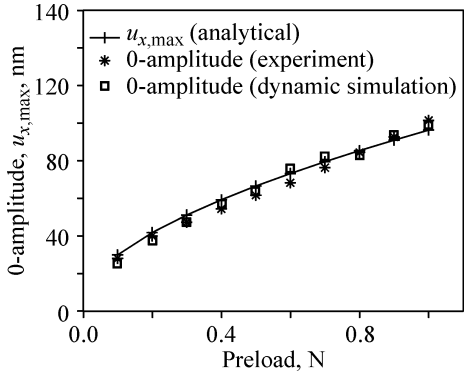


**Fig. 7.** Dependency of $u_{x,\max}$ (analytical) and 0-amplitude (experiment and dynamic simulation) on preload $F_p$. Roughness $H = 0.7$, $Q_{1D} = 4.4478 \times 10^{-4}$, $h = 1.1221$ μm.

The graphs in Fig. 7 show very good agreement between $u_{x,\max}$ and the 0-amplitude (both the dynamic simulation and experiment). This result consolidates the explanation that the 0-amplitude or presliding is closely related to $u_{x,\max}$, the maximum tangential displacement before the whole contact starts to slide. Furthermore, the numerical simulation of the tangential contact with roughness by the method of dimensionality reduction described in Sect. 3 matches very well with the theoretical explanation and experimental data. This shows a good quality of the introduced friction model.

## 5. CONCLUSIONS

In this work, numerical simulations of stick-slip microdrive are studied. By applying the method of dimensionality reduction, the microscopic contacts in the frictional driving elements have been considered as rough surfaces. The new friction model presented in [10] was extended by considering roughness influences of the runner surface. The tangential dynamic behavior of the rough contact was modeled and simulated in combination with the macroscopic model of the drive runner. As the first approximation, the parameters for roughness were empirically chosen. The quality of the presented model has been validated by comparing numerical and experimental results in which a strong agreement for the 0-amplitude is obtained. However, the simulations of generated force are still qualitative. It has been concluded that when considering the contact roughness, the 0-amplitude can be much better explained and predicted. This relates closely to maximum tangential displacement which has been theoretically analyzed and validated.

## REFERENCES


1. Pohl, D.W., Dynamic Piezoelectric Translation Devices, *Rev. Sci. Ins*., 1987, vol. 58(1), pp. 54–57.
2. Zhang, Z.M., An, Q., Li, J.W., and Zhang, W.J., Piezoelectric Friction-Inertia Actuator—a Critical Review and Future Perspective, *Int. J. Adv. Manu. Tech*., 2012, vol. 62(5–8), pp. 669–685.
3. Nguyen, H.X., Edeler, C., and Fatikow, S., Modeling of Piezo-Actuated Stick-Slip Micro-drives: An Overview, *Adv. Sci. Tech.: Proc. 4th Int. Conf. Smart Mater., Struct. Syst*., 2012, vol. 81, pp. 39–48.
4. Dahl, P.R., A Solid Friction Model, *Aerosp. Coop. El Segundo CA*, 1968, no. ADA041920.
5. de Wit, C., Olsson, H., Astrom, K., and Lischinsky, P., A New Model for Control of Systems with Friction, *IEEE Trans. Autom. Contr*., 1995, vol. 40, pp. 419–425.
6. Breguet, J.-M., Stick and Slip Actuators, *PhD Dissertation*, Zurich: Swiss Federal Institute of Technology ETH Zurich, 1998.
7. Dupont, P., Hayward, V., Armstrong, B., and Altpeter, F., Single State Elastoplastic Friction Models, *IEEE Trans. Auto. Contr.*, 2002, vol. 47, pp. 787–792.
8. Peng, J.Y. and Chen, D.B., Modeling of Piezoelectric-Driven Stick-Slip Actuators, *IEEE/ASME Trans. Mechatron*, 2010, vol. 99, pp. 1–6.
9. Edeler, C., Modellierung und Validierung der Krafterzeugung mit Stick-Slip-Antrieben für nanorobotische Anwendungen, *PhD Dissertation*, Oldenburg: Carl von Universität Oldenburg, 2011.
10. Nguyen, H.X., Teidelt, E., Popov, V.L., and Fatikow, S., Modeling and Waveform Optimization of Stick-Slip Microdrives by the Method of Dimensionality Reduction, Submitted for publication in *J. Arch. App. Mech.*
11. Popov, V.L. and Psakhie, S.G., Numerical Simulation Methods in Tribology, *Tribol. Int*., 2007, vol. 40, pp. 916–923.
12. Geike, T. and Popov, V.L., Mapping of Three-Dimensional Contact Problems into One Dimension, *Phys. Rev.*, 2007, vol. 76, p. 036710.
13. Geike, T. and Popov, V.L., Reduction of Three-Dimensional Contact Problems to One-Dimensional Ones, *Tribol. Int*., 2007, vol. 40, pp. 924–929.
14. Heß, M., Über die exakte Abbildung ausgewählter dreidimensionaler Kontakte auf Systeme mit niedrigerer räumlicher Dimension, *PhD Dissertation*, Göttingen: Cuvillier-Verlag, Technische Universität Berlin, 2011.
15. Popov, V.L., Basic Ideas and Applications of the Method of Reduction of Dimensionality in Contact Mechanics, *Phys. Mesomech*., 2012, vol. 15, no. 5–6, pp. 254–263.
16. Popov, V.L., Method of Reduction of Dimensionality in Contact and Friction Mechanics: A Linkage between Micro and Macro Scales, *Friction*, 2013, vol. 1(1), pp. 41–62.
17. Pohrt, R., Popov, V.L., and Filippov, A.E., Normal Contact Stiffness of Elastic Solids with Fractal Rough Surfaces, *Phys. Rev. Lett*., 2012, vol. 108, p. 104301.
18. Pohrt, R. and Popov, V.L., Normal Contact Stiffness of Elastic Solids with Fractal Rough Surfaces for One- and Three-Dimensional Systems, *Phys. Rev. E*, 2012, vol. 86, p. 026710.
19. Pohrt, R. and Popov, V.L., Contact Mechanics of Rough Spheres: Crossover from Fractal to Hertzian Behavior, *Adv. Tribol*., 2013, p. 974178.
20. Popov, V.L. and Heß, M., *Methode der Dimensionsreduktion in Kontaktmechanik und Reibung Eine Berechnungsmethode im Mikro- und Makrobereich*, Berlin: Springer, 2013.
21. Grzemba, B., Pohrt, R., Teidelt, E., and Popov, V.L., Maximum Micro-Slip in Tangential Contact of Randomly Rough Self-affine Surfaces, *Wear*, 2014, vol. 309, no. 1–2, pp. 256–258.